

The First Population II Stars Formed in Externally Enriched Mini-halos

Britton D. Smith^{1*}, John H. Wise², Brian W. O’Shea^{3†}, Michael L. Norman⁴,
and Sadegh Khochfar¹

¹*Institute for Astronomy, University of Edinburgh, Royal Observatory, Edinburgh EH9 3HJ, UK*

²*Center for Relativistic Astrophysics, Georgia Institute of Technology, 837 State Street Atlanta, GA 30332, USA*

³*Department of Physics & Astronomy, Michigan State University, East Lansing, MI 48824, USA*

⁴*Center for Astrophysics and Space Sciences, University of California at San Diego, La Jolla, CA 92093, USA*

9 April 2018

ABSTRACT

We present a simulation of the formation of the earliest Population II stars, starting from cosmological initial conditions and ending when metals created in the first supernovae are incorporated into a collapsing gas-cloud. This occurs after a supernova blast-wave collides with a nearby mini-halo, inducing further turbulence that efficiently mixes metals into the dense gas in the center of the halo. The gas that first collapses has been enriched to a metallicity of $Z \sim 2 \times 10^{-5} Z_{\odot}$. Due to the extremely low metallicity, collapse proceeds similarly to metal-free gas until dust cooling becomes efficient at high densities, causing the cloud to fragment into a large number of low mass objects. This external enrichment mechanism provides a plausible origin for the most metal-poor stars observed, such as SMSS J031300.36-670839.3, that appear to have formed out of gas enriched by a single supernova. This mechanism operates on shorter timescales than the time for low-mass mini-halos ($M \leq 5 \times 10^5 M_{\odot}$) to recover their gas after experiencing a supernova. As such, metal-enriched stars will likely form first via this channel if the conditions are right for it to occur. We identify a number of other externally enriched halos that may form stars in this manner. These halos have metallicities as high as $0.01 Z_{\odot}$, suggesting that some members of the first generation of metal-enriched stars may be hiding in plain sight in current stellar surveys.

Key words: cosmology, hydrodynamics, radiative transfer, methods: numerical, galaxies: star formation

1 INTRODUCTION

The physical processes relevant to star formation have conspired to produce stars of predominantly low mass for most of the history of the Universe. The stellar initial mass function (IMF) appears to be so robust to variations in environment that debate over its universality primarily concerns whether the statement “the IMF is universal” should include the word *almost*. Excellent reviews of this subject have been provided by Kroupa (2002) and more recently, Bastian et al. (2010). The one notable exception to the universality of the IMF is the case of metal-free (Population III or Pop III) stars. The mid 2000s was a boom for quality reviews of this subject (Barkana & Loeb 2001; Bromm & Larson 2004; Ciardi & Ferrara 2005; Glover 2005; Ripamonti & Abel 2006; Bromm et al. 2009). In short, neutral metal-free gas cools very inefficiently as it col-

lapses, resulting in Jeans mass-scale fragments that are of the order of thousands of M_{\odot} . Early simulations found that this resulted in the formation of only one (Abel et al. 2002; Bromm et al. 2002; Yoshida et al. 2006; O’Shea & Norman 2007) or two (Turk et al. 2009; Stacy et al. 2010) dense cores that were free to accrete from this massive envelope and grow uncontested. More recent simulations have found that the disks surrounding the massive, central core can be unstable to fragmentation, potentially providing a channel for lower mass Pop III stars (Clark et al. 2011; Greif et al. 2011; Stacy & Bromm 2014). However, simulations that follow the late-time accretion onto the central object find that they will grow to be 10s to 1000s of M_{\odot} in final size (Hosokawa et al. 2011; Hirano et al. 2014, 2015; Susa et al. 2014), making it quite clear that the Pop III star formation mode is, at a bare minimum, unquestionably distinct. Even on the low mass end of the Pop III IMF, Hartwig et al. (2015) claim that the existing sample size of low-metallicity star surveys in the Milky Way can already rule out the existence of metal-free stars below $0.65 M_{\odot}$ with 95% certainty, barring enrichment via accretion of metals from the interstellar medium (Johnson 2014).

* e-mail:brs@roe.ac.uk

† Department of Computational Mathematics, Science, and Engineering; Lyman Briggs College; and the Joint Institute for Nuclear Astrophysics, Michigan State University, East Lansing, MI 48824, USA

Following naturally from the idea that the first stars to ever form in the Universe represent an exception to the universal stellar IMF is the question of how this necessary transition in star formation modes took place. The Universe was forever changed when supernovae from the first stars created the first metals, whose introduction to star-forming gas enhanced its ability to cool and fragment. From this argument of increased cooling and fragmentation, two “critical metallicities” have been found for yielding a significant departure from the thermal evolution of collapsing metal-free gas. At low densities¹, $\sim 10^{4-6} \text{ cm}^{-3}$, fine-structure lines of atomic C and O allow collapsing gas to continue to cool past the limitations of metal-free coolants (primarily H_2) at a metallicity of $\sim 10^{-3.5} Z_\odot$ (Bromm & Loeb 2003). At much higher densities, $\sim 10^{12-14} \text{ cm}^{-3}$, dust emission can induce a sharp cooling phase when the metallicity is only $\sim 10^{-5.5} Z_\odot$, assuming the dust-to-gas ratio scales with the gas-phase metallicity (Omukai 2000; Omukai et al. 2005; Schneider et al. 2006). Three-dimensional hydrodynamic simulations have shown that the cooling phases that occur when these critical metallicities are reached can indeed trigger fragmentation in their associated density regimes (Bromm et al. 2001); Smith & Sigurdsson (2007); Smith et al. (2009); Meece et al. (2014) for the atomic and Clark et al. (2008); Dopcke et al. (2011, 2013) for the dust critical metallicity). However, it has also been found that the ability of gas to actually fragment depends sensitively on the initial conditions, no matter what the metallicity (Jappsen et al. 2007, 2009a,b; Meece et al. 2014). In particular, without a small amount of turbulence to create seed perturbations, monolithic collapse cannot be avoided (Meece et al. 2014). Thus, it seems that further progress requires understanding the true physical conditions in which the first metal-enriched stars formed.

This paper is the first in a series that will investigate the range of scenarios in which star formation producing the near-universal IMF first occurred. Noting the ability of Pop III stars to completely evacuate their host mini-halos through ionizing radiation and supernovae (Whalen et al. 2004, 2008; Kitayama & Yoshida 2005), a number of recent works have sought to characterize the required conditions for metal-enriched star formation in terms of (i) incorporation of metals via hierarchical structure formation into more massive halos (Greif et al. 2007; Wise & Abel 2008; Greif et al. 2010; Wise et al. 2012b; Safranek-Shrader et al. 2014a,b, 2015) or (ii) fallback onto the original halo after a recovery period (Ritter et al. 2012; Jeon et al. 2014; Ritter et al. 2014). These are both viable scenarios, but because they typically involve stars forming with metallicities of $Z \gtrsim 10^{-3} Z_\odot$, they are unlikely to be the formation mechanisms of the most metal-poor stars observed with $[\text{Fe}/\text{H}]^2 \sim -5.5$ (Norris et al. 2013). Here, we report on a third scenario for low-metallicity star formation, whereby mini-halos that have yet to form stars are externally enriched by a Pop III supernova from a nearby halo. We note that while this channel has not before been shown conclusively to give rise Pop II-like stars, it was previously suggested as a possibility by Greif et al. (2010), who found a halo similar to what we describe here but did not have the ability to follow the collapse and fragmentation. This is also similar to the “gravitational enrichment” scenario proposed by Maio et al. (2011). The simulations presented here are the first of their kind to follow the metal creation, non-uniform enrichment of the surrounding medium, and eventual collapse to high density within a single,

coherent run. As such, they represent a significant leap forward in understanding the origins of the first low-mass stars.

The paper is organized as follows. In Section 2, we describe the simulation code and the setup of the simulations. We present the results in Section 3. We first describe the general evolution of the simulation in Section 3.1. We then investigate the process by which the Pop II star-forming halo is enriched through turbulent mixing with the supernova blast-wave in Section 3.2. Following this, we characterize the physical conditions within the star-forming cloud, including fragmentation, the role of dust, and the velocity structure of the gas in Section 3.3. We conclude the results in Section 3.4 by estimating how often stars will form via this external enrichment mechanism. In Section 4, we discuss the implications of these results and some limitations of our work. Finally, we summarize the results and discuss the ways in which this work may be extended in Section 5.

2 METHODS

2.1 Simulation Code

2.1.1 The ENZO Framework

We use the ENZO³ simulation code (Bryan et al. 2014) for all simulations presented here. ENZO is an open-source, adaptive mesh refinement + N-body cosmological simulation code that has been heavily used for simulating cosmological structure formation over a large range of scales. ENZO has been employed by numerous works to study high-redshift structure formation, including Pop III star formation (Abel et al. 2002; O’Shea et al. 2005; O’Shea & Norman 2007, 2008; Turk et al. 2009, 2010, 2011a, 2012), low-metallicity star formation (Smith & Sigurdsson 2007; Smith et al. 2009; Meece et al. 2014), and the first galaxies (Wise et al. 2012a,b; Xu et al. 2013; Wise et al. 2014; Chen et al. 2014). All functionality of the ENZO code is thoroughly detailed in Bryan et al. (2014), but we briefly describe the most relevant machinery here. ENZO uses a block-structured adaptive mesh refinement (AMR) framework (Berger & Colella 1989) to solve the equations of ideal hydrodynamics in an Eulerian frame, with multiple hydrodynamic solvers implemented. For these simulations, we use the Piecewise Parabolic Method of Woodward & Colella (1984). This is coupled to an N-body adaptive particle-mesh gravity solver (Efsthathiou et al. 1985; Hockney & Eastwood 1988). When ionizing radiation fields from stellar sources are present (described below in Sections 2.1.2 and 2.1.3), we also use the MORAY adaptive ray-tracing radiation transport method of Wise & Abel (2011). The AMR framework dynamically creates (refines) and destroys (de-refines) grid patches at varying levels of resolution based on multiple criteria. This enables the study of astrophysical phenomena with processes occurring over a large range of spatial and temporal scales. We list the refinement criteria employed in this work below in Section 2.2.

2.1.2 Chemistry and Cooling

We use a chemistry model that follows the non-equilibrium evolution of 12 primordial species (H , H^+ , He , He^+ , He^{++} , e^- , H_2 , H_2^+ , H^- , D , D^+ , and HD) following the method originally described in Anninos et al. (1997) and Abel et al. (1997). This method has been updated to include H_2 formation via three-body reactions (Abel

¹ Unless stated otherwise, all densities and number densities are assumed to be in the proper frame.

² $[\text{Fe}/\text{H}]$ refers to the \log_{10} of the iron abundance relative to the sun.

³ <http://enzo-project.org/>, changeset 7b5518a63792

et al. 2002), H₂ formation heating, and collisionally-induced H₂ emission (Turk et al. 2009). We include the effects of ionizing radiation from Pop III stars by coupling the chemistry network to the MORAY radiation transport solver (Wise & Abel 2011). We also include optically thin, H₂ photo-dissociating Lyman-Werner (LW) radiation with an intensity decreasing as r^{-2} from the source together with the H₂ ‘‘Sobolev-like’’ self-shielding model of Wolcott-Green et al. (2011).

Just as primordial chemistry appears simple enough to allow for the hope that it can be computed entirely without limiting assumptions in a large, three-dimensional simulation, the introduction of the first heavy elements by Pop III supernovae adds a level of complexity to the Universe that crushes that hope. We calculate the cooling from gas-phase metals following the method of Smith et al. (2008), which uses multidimensional tables pre-computed with the photoionization code, CLOUDY⁴ (Ferland et al. 2013). For simplicity, we assume the cooling from metals corresponds to a solar abundance pattern. When Pop III stars are present, we use a four-dimensional cooling table that spans the parameter space of density, metallicity, temperature, and electron fraction to account for the increased ionization from the radiation field. When metal-enriched gas begins to reach high densities, we switch to a table that covers only density, metallicity, and temperature, but was computed up to higher densities than the four-dimensional table.

In addition to gas-phase chemistry and cooling, we also take into account the contribution of dust grains, which provide an additional channel for H₂ formation and an efficient cooling mechanism at high densities. The implementation used here closely follows the work of Omukai (2000) and Omukai et al. (2005), with modifications motivated by Dopcke et al. (2011), and is detailed in Meece et al. (2014). The primary assumption to note is that the gas-to-dust ratio scales with the metallicity and that the grain size distribution and abundances follow the model of Pollack et al. (1994), as in Omukai (2000).

2.1.3 Population III Star Formation and Feedback

We model the formation and feedback of Pop III stars with the method presented in Wise et al. (2012b). During the simulation, we insert a Pop III star particle into a grid cell where the following conditions are met:

- (i) The *proper* baryon number density exceeds 10^7 cm^{-3} .
- (ii) The gas flow is convergent ($\nabla \cdot \mathbf{v}_{\text{gas}} < 0$).
- (iii) The molecular hydrogen mass fraction, $f_{\text{H}_2} \equiv (\rho_{\text{H}_2} + \rho_{\text{H}_2^+})/\rho_{\text{b}}$, exceeds 5×10^{-4} , (where ρ_{H_2} , $\rho_{\text{H}_2^+}$, and ρ_{b} are the neutral molecular hydrogen, singly-ionized molecular hydrogen, and the total baryon densities, respectively).
- (iv) The metallicity is less than $10^{-6} Z_{\odot}$. If the metallicity is greater than this, we will explicitly follow the collapse.

These physical conditions are typical of metal-free molecular clouds nearing the end of the ‘loitering’ phase observed in simulations of Pop III star formation (Abel et al. 2002; Bromm et al. 2002; Yoshida et al. 2006; O’Shea & Norman 2007; Turk et al. 2009). In the simulations here, we adopt a delta function at $M = 40 M_{\odot}$ for the IMF of the Pop III star particles. When a star particle is created, the mass of the star is removed evenly from a spherical region containing twice the particle mass. Once

formed, the star particle isotropically emits ionizing and LW radiation following the stellar evolution models of Schaerer (2002) with no mass loss. Following this, the main-sequence lifetime of the $40 M_{\odot}$ Pop III star is 3.86 Myr. Furthermore, we treat the star as a radiation point source, whose spectrum is discretised into four energy groups with the following photon energies and luminosities: (i) hydrogen ionizing photons with $E = 28 \text{ eV}$ and $L_{\gamma} = 2.47 \times 10^{49} \text{ s}^{-1}$; (ii) helium singly-ionizing photons with $E = 30 \text{ eV}$ and $L_{\gamma} = 1.32 \times 10^{49} \text{ s}^{-1}$; (iii) helium doubly-ionizing photons with $E = 58 \text{ eV}$ and $L_{\gamma} = 8.80 \times 10^{46} \text{ s}^{-1}$; (iv) H₂ dissociating photons with $L_{\gamma} = 2.90 \times 10^{49} \text{ s}^{-1}$ (Schaerer 2002). The ionizing radiation field is transported using the MORAY radiation transport solver (Wise & Abel 2011). As stated previously, we model the H₂ photo-dissociating LW flux to be declining simply as r^{-2} with a self-shielding correction.

When the Pop III star’s main-sequence lifetime ends, it explodes as a standard Type II core-collapse supernova with an explosion energy of 10^{51} ergs. Following the calculations of Nomoto et al. (2006), the supernova has a metal yield of $11.19 M_{\odot}$ and a total ejecta mass of $38.6 M_{\odot}$. We model the blast-wave by depositing the explosion energy and mass into a sphere with a radius of 10 proper pc that has been smoothed at its surface to improve numerical stability (Wise & Abel 2008). We choose this radius as it marks the end of the free-expansion phase of the supernova. At the time of instantiation, the blast-wave is extremely well-resolved and agrees with the Sedov-Taylor solution.

2.2 Simulation Setup

We initialize the simulation with a 500 kpc/h comoving box at $z = 180$ using the MUSIC initial conditions generator (Hahn & Abel 2011) with the WMAP 7 best-fit cosmological parameters, $\Omega_m = 0.266$, $\Omega_{\Lambda} = 0.732$, $\Omega_b = 0.0449$, $H_0 = 71.0 \text{ km/s/Mpc}$, $\sigma_8 = 0.801$, and $n_s = 0.963$ (Komatsu et al. 2011), and using a Eisenstein & Hu (1999) transfer function and second-order Lagrangian perturbation theory. We first run an exploratory dark matter-only simulation with 512^3 particles to $z = 10$. We then use the ROCKSTAR halo finder (Behroozi et al. 2013a, interfaced through the YT analysis toolkit) and the CONSISTENT-TREES merger tree algorithm (Behroozi et al. 2013b) to locate a halo with total mass (at $z = 10$) of $\sim 10^7 M_{\odot}$ and the highest number of unique progenitor halos with $M \geq 10^6 M_{\odot}$. The second of these criteria was added to maximize the number of Pop III stars formed, and hence the amount of metals produced, by the time the halo has reached $z = 10$. The halo selected, referred to from here on as the ‘‘target halo’’, has a total mass at $z = 10$ of $1.7 \times 10^7 M_{\odot}$ and 4 unique progenitors with $M \geq 10^6 M_{\odot}$ (and 7 with $M \geq 5 \times 10^5 M_{\odot}$).

We generate the initial conditions for the primary simulation using the same configuration and random seed as the exploratory run, including baryons as well as dark matter, and with two additional levels of telescoping refinement around the target halo. The high resolution region is a rectangular prism minimally containing all of the dark matter particles that end up within 3 virial radii of the target halo. It has an effective resolution of 2048^3 , corresponding to a comoving spatial resolution of 0.244 kpc/h , and a baryon (dark matter) mass resolution of $0.259 M_{\odot}$ ($1.274 M_{\odot}$).

We evolve the simulation from $z = 180$ with the physics described in Section 2.1, allowing adaptive mesh refinement to occur only within the high resolution region. Grid cells are adaptively refined by factors of 2 in each dimension when any of the following conditions exist:

⁴ <http://nublado.org/>

(i) The dark matter mass within a grid cell is greater than 4 times the initial mass (i.e., when more than 4 dark matter particles are in the same cell).

(ii) The gas mass within a grid cell is greater than 4 times the mean baryon mass per cell on the root grid multiplied by a factor, $2^{-0.2L}$, where L is the refinement level.

(iii) The local Jeans length is resolved by less than 64 cells.

The negative exponential factor used with the baryon mass criterion ensures that refinement is mildly super-Lagrangian. Requiring that the local Jeans length be resolved by at least 64 cells (a factor of 16 higher than the criterion put forth by Truelove et al. 1997) has been shown to be necessary to guarantee that fragmentation is purely physical in origin (Federrath et al. 2011; Meece et al. 2014).

We place no strict limit on the maximum number of AMR levels in the simulation. However, in practice, the simulation typically reaches 15 levels of refinement before forming a Pop III star, corresponding to a comoving spatial resolution of 0.03 pc/h. Finally, we stop the simulation once gas with metallicity of at least $10^{-6} Z_{\odot}$ reaches a maximum number density of $\sim 10^{13} \text{ cm}^{-3}$. This occurs at 27 levels of refinement, for a spatial resolution of approximately 1.5 AU/h comoving. As discussed in Section 3.3, after the first Pop III supernova occurs, we start a second simulation from this point with all physics the same except without dust grains.

We run the simulations on the Blue Waters supercomputer at the National Center for Supercomputing Applications on 64 nodes of the machine, using 8 cores/node. The primary run took roughly 42 days, with a total computational cost of approximately 64,000 node-hours. For all of the analysis and images presented here, we use the YT⁵ simulation analysis toolkit (Turk et al. 2011b).

3 RESULTS

3.1 Qualitative Evolution

The two simulations proceed identically until the collapse of metal-enriched gas first occurs at $z \sim 16.6$, at which time their behaviors diverge due to the presence/absence of dust grains. The qualitative evolution prior to this is as follows. From here on, we refer to the halo in which metal-enriched collapse occurs as the “action halo.” Within the high resolution region, two Pop III stars form in separate halos, shine, and explode. The evolution of the halos hosting Pop III stars agrees well with earlier studies of this scenario (Whalen et al. 2004, 2008; Kitayama & Yoshida 2005). As the halos are only a few hundred thousand M_{\odot} , the Pop III star is able to completely photo-evaporate them. The central baryon density is reduced to roughly 0.1 cm^{-3} before the core-collapse supernova occurs and totally evacuates the gas from the halo. As in Whalen et al. (2008), the supernova shockwave has a density of just under 1 cm^{-3} and catches up with the expanding shell of the HII region within a few million years of the explosion. This collision enhances the density by a factor of roughly 10 to 30, after which the shell proceeds to break up into small knots. These knots eventually dissolve, but they carry metals out into the intergalactic medium (IGM), creating finger-like structures in the metal field, which are clearly visible in the upper-right panel of Figure 13. The first of the two Pop III stars, forming at $z \sim 23.7$, has no influence on the action halo. The second Pop III star forms at $z \sim 18.2$ (~ 66.6 Myr later) and is solely responsible for enriching the action halo. By the time of gas

collapse in the action halo, the supernova blast-waves from each of the two Pop III-hosting halos (separated by ~ 3.4 kpc) are still ~ 1 kpc from a collision. In another version of this simulation carried beyond this point, we find that the blast-waves meet at $z \sim 14$ (~ 65 Myr in the future).

Figure 1 displays the sequence of events immediately leading up to metal-enriched collapse. The action halo is roughly 200 pc away from the second Pop III star when it forms. The Pop III star photo-ionizes its host halo and causes a slight compression of the gas in the filament hosting the action halo. This is visible in the third row of Figure 1. Prior to this, the action halo has a relatively low central baryon fraction, about a few percent of the cosmic baryon to dark matter ratio. Over the main sequence lifetime of the star, the central density of the action halo increases by a factor of a few, raising the baryon fraction to over 10% of Ω_b/Ω_{dm} . The gas in the action halo remains almost entirely neutral, with an HII fraction of about 10^{-4} in the central 10 pc, increasing to 10^{-2} at 50 pc. Approximately 6 Myr after the Pop III supernova occurs, the blast-wave encounters the action halo moving in the opposite direction. At this point, the action halo has a virial mass of $\sim 3 \times 10^5 M_{\odot}$. Turbulence produced by the virialization of the action halo (Wise & Abel 2007; Greif et al. 2008) and the passing of the blast-wave allows metals from the supernova to mix into the core of the action halo. It also happens that the blast-wave encounters the action halo just prior to colliding with the HII region shell and thus meets the halo with an enhanced density. This process is illustrated in Figure 2. Finally, runaway collapse occurs in the center of the action halo where the metallicity has reached $\sim 2 \times 10^{-5} Z_{\odot}$. While this is happening, the action halo and the gas-depleted Pop III halo continue on a near collision course. By the time collapse occurs, the two halos have passed close enough that the halo finder considers them to be a single halo, although distinct cores are still visible.

3.2 Enrichment of the Action Halo

The Pop III supernova blast-wave carries with it $11.19 M_{\odot}$ of metals and impacts the action halo about 6 Myr after the explosion. Figure 3 shows the metallicity as a function of radius from the metal-enriched gas cloud at the time of final collapse. At the scale of 10–100 pc, gas exists from zero metallicity up to roughly $10 Z_{\odot}$ as spherical shells of this size are sampling the blast wave itself as well as regions that have yet to be encountered. Within a few pc of the dense cloud, no pristine gas exists and the metallicity is as high as $10^{-3} Z_{\odot}$. Inside of 0.01 pc, the metallicity is nearly constant at $\sim 2 \times 10^{-5} Z_{\odot}$. To understand this, we compare the timescales for collapse and mixing in Figure 4. The collapse timescale is the free-fall time, given by

$$t_{\text{ff}} = \sqrt{\frac{3\pi}{32G\rho}}, \quad (1)$$

where ρ is the gas density. We estimate the mixing timescale as the vortical time (e.g., Ritter et al. 2014),

$$t_{\text{vort}} \simeq \frac{2\pi}{|\nabla \times \mathbf{v}|}, \quad (2)$$

where the factor of 2π accounts for a full rotation of an eddy. The mixing timescale is shorter than the free-fall time outside of a few pc and, thus, mixing occurs here. However, at $r \sim 1$ pc, the free-fall time is slightly shorter than the vortical time, allowing the gas to momentarily collapse faster than the rate at which additional metals can be brought in from the surrounding medium. We expect the rate of collapse to be regulated by the free-fall time in this regime since

⁵ <http://yt-project.org>

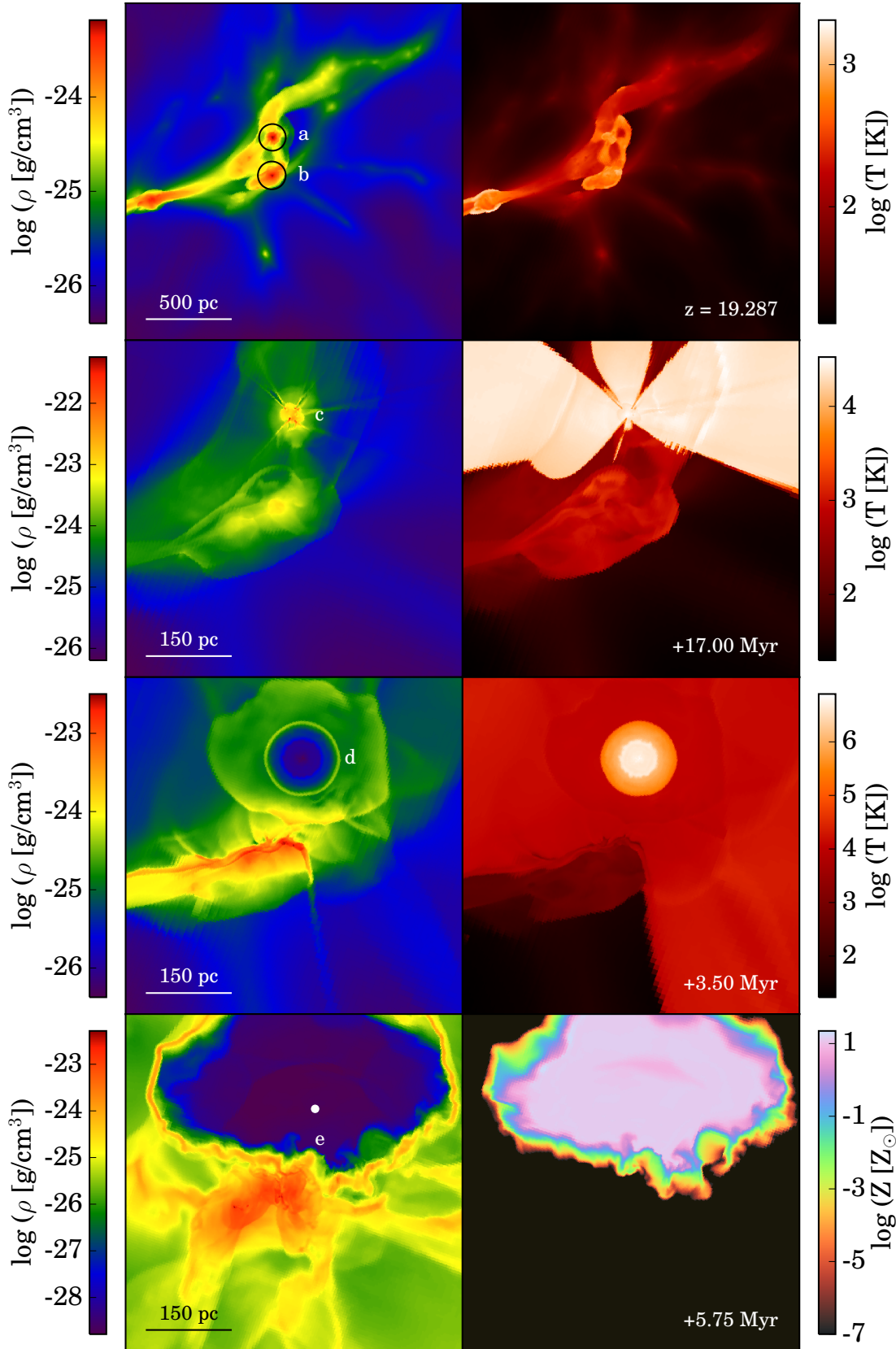


Figure 1. Slices illustrating the large-scale evolution of the simulation prior to the collapse of metal-enriched gas, oriented such that it contains the vector connecting the Pop III star to the rough center of the action halo. Letters indicate the following: at $z = 19.287$ a) the Pop III star-forming halo, b) the halo in which metal-enriched gas will collapse (i.e., the action halo), c) the Pop III star begins shining ~ 17 Myr later, d) the Pop III star explodes in a core-collapse supernova ~ 4 Myr later, and e) the supernova blastwave collides with the action halo. The black circles in the top-left panel indicate the virial radii of the Pop III (79 pc) and action (82 pc) halos. The white circle in the bottom-left panel shows the location of the evacuated Pop III star halo.

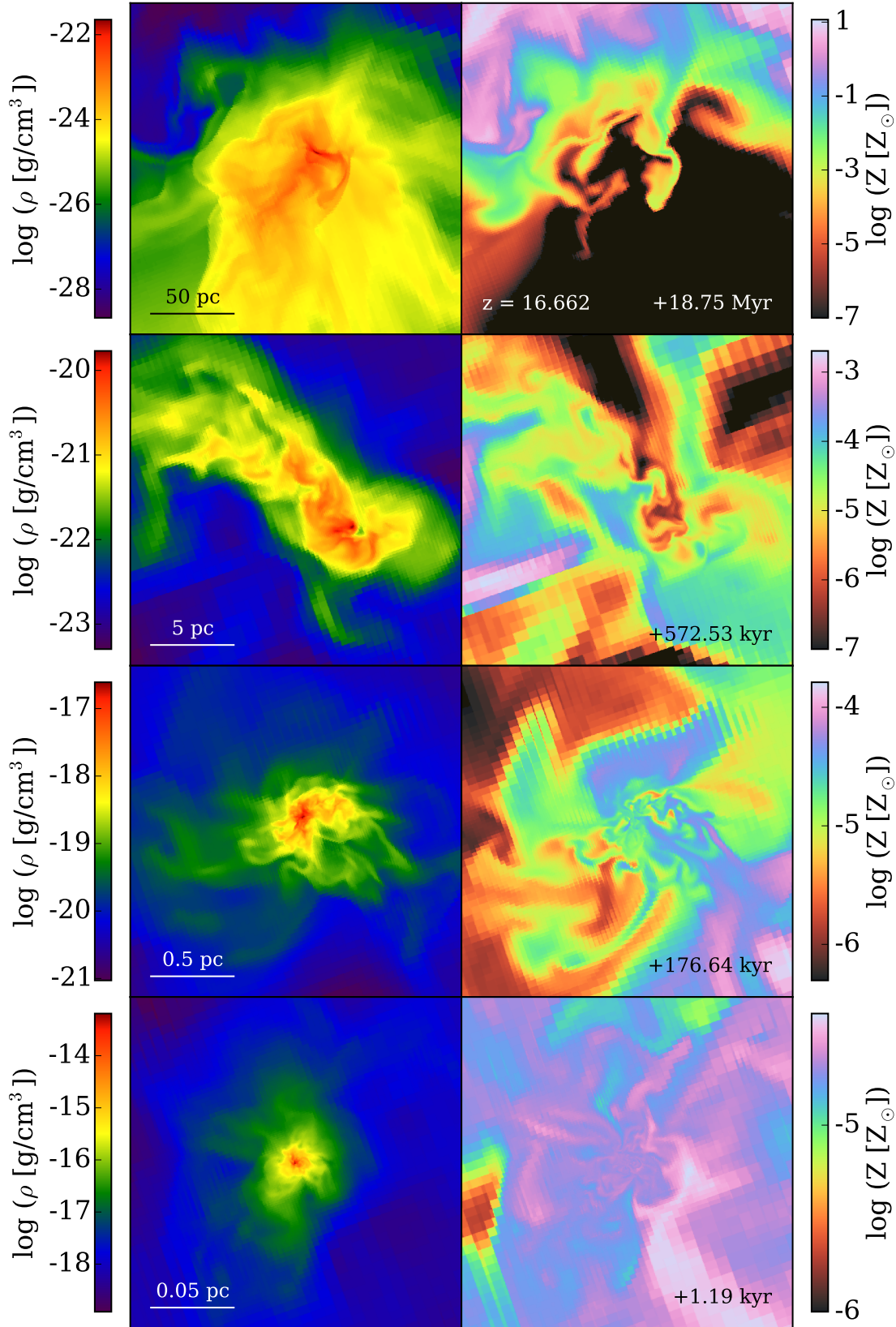


Figure 2. Slices showing the turbulent mixing of the metal-enriched blastwave with the action halo. The top panels show the state of the simulation ~ 18.75 Myr after the bottom panel of Figure 1. Here, as in Figure 1, the scale bars show distances in the proper frame and the slicing plane contains both the Pop III star and action halo center.

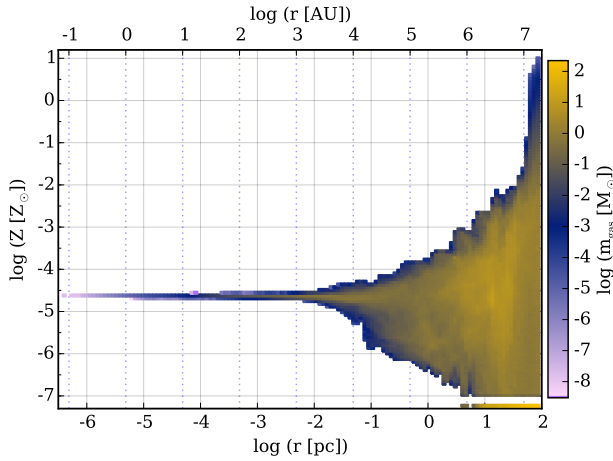


Figure 3. Phase plot showing the mass of gas in bins of metallicity and radius from the central core for the simulation with dust. All gas with metallicity $Z < 10^{-7} Z_{\odot}$ is combined and shown in the small strip at the bottom. This gas is entirely at $\log(r/\text{pc}) > 0.5$; all gas within that radius has been enriched to a higher level.

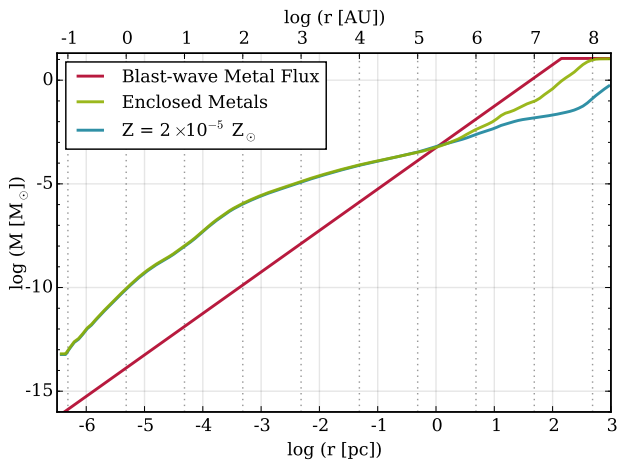


Figure 5. The red line shows the maximum metal mass that would have passed through a circle of radius, r , in the absence of mixing after the blast-wave has reached the action halo. The green line shows the enclosed mass of metals within the cloud and blue shows the enclosed metal mass corresponding to a constant metallicity of $2 \times 10^{-5} Z_{\odot}$. The flattening of the red line indicates the total metal yield of the supernova ($11.19 M_{\odot}$). All of the metals are within 500 pc of the center, as shown by the flattening of the green line.

the cooling time is equivalent to or shorter than the free-fall time here.

Further evidence of the mixing process can be seen in Figure 5, where we compare the enclosed mass in metals to the maximum flux of metals carried by the blast-wave. Under the assumptions that the blast-wave is spherical and that all of the metals are carried in the front, the mass in metals that would have passed through a hole of radius, r , is given by

$$M_{\text{flux}} = M_{\text{SN}} \frac{r^2}{4d^2}, \quad (3)$$

where the metal yield of the supernova, M_{SN} , is $11.19 M_{\odot}$, and the proper distance between the halo and the origin of the blast-wave,

d , is ~ 70 pc. Where the enclosed metal mass is greater than the amount carried by the blast-wave, turbulence has acted to enhance the metal mass over what the blast-wave could have maximally deposited without mixing. We also show in Figure 5 the mass in metals corresponding to the constant metallicity of the inner cloud. In the region where this curve diverges from the true enclosed metal mass, mixing is ongoing and continues to increase the metallicity of the gas beyond the point at which the metallicity is frozen out by rapid collapse. We note here for the sake of novelty that the total mass in metals within 1 pc of the center of the dense cloud is only about half the mass of Jupiter.

Cen & Riquelme (2008) study the mixing of metals into pristine halos impacted by supernova blast-waves using idealized simulations. In the configuration most similar to the scenario here, ($M_{\text{halo}} \sim 3 \times 10^5 M_{\odot}$, $v \sim 11$ km/s,) they find that very little mixing occurs with a majority of the dense gas in the halo remaining at a metallicity less than 3% of the blast-wave. However, there are some key differences between the conditions we observe in the action halo and the simulations of Cen & Riquelme (2008). The minimum halo mass simulated in Cen & Riquelme (2008) was $10^6 M_{\odot}$, roughly 3 times more massive than the action halo. More importantly, the halos in Cen & Riquelme (2008) were initialized with the gas in hydrostatic equilibrium with no internal motion. As Figures 1 and 2 show, the action halo is in a highly perturbed state immediately prior to impact, having its turbulence first stirred during virialization and then being eroded by the Pop III stellar radiation. This is supported by the results of Richardson et al. (2013), who perform a similar study to that of Cen & Riquelme (2008), but using realistic mini-halos with $M \sim 10^6 M_{\odot}$ extracted from a cosmological simulation. Whereas Cen & Riquelme (2008) find that most of the material in idealized halos of this size remains pristine, Richardson et al. (2013) observe that most of the halo gas is enriched to $\sim 3\%$ of the metallicity of the blast-wave. Finally, we note that while enough metals are mixed into the collapsing gas to constitute a transition to low-mass star formation in the cloud, the mixing should not be considered very efficient. At the 1 pc scale where free-fall collapse freezes in the metallicity of the dense gas, Figure 3 shows that the range in metallicity is nearly 3 orders of magnitude, with metallicities present up to 10 times higher than that of the dense cloud.

3.3 Physical Conditions of The First Pop II Stars

The first Pop II star forming cloud within the simulation has a nearly constant metallicity of $Z \sim 2 \times 10^{-5} Z_{\odot}$. In Figure 6, we show density projections progressively zooming in to the central density peak of the final output of the simulation. Not surprisingly, we see no evidence of fragmentation at densities much lower than the maximum reached in the simulation, as gas-phase metal cooling has almost no effect at such low metallicities (Omukai 2000; Omukai et al. 2005; Smith et al. 2009; Meece et al. 2014). However, in the central 100 AU, we observe significant fragmentation at densities, $\rho \gtrsim 10^{-12} \text{ g/cm}^3$, where the cooling from dust grains becomes efficient (Omukai 2000; Omukai et al. 2005; Schneider et al. 2006; Clark et al. 2008; Dopcke et al. 2011; Meece et al. 2014). To confirm that the fragmentation that occurs is due to the effects of dust, we run a second simulation without dust starting from the moment following the first Pop III supernova. In the lower-right panel of Figure 6, we show the corresponding central, dense region, which has undergone significantly less fragmentation.

To quantify this notion, we run a clump-finding algorithm to identify bound clumps within 50 pc of the peak density in both sim-

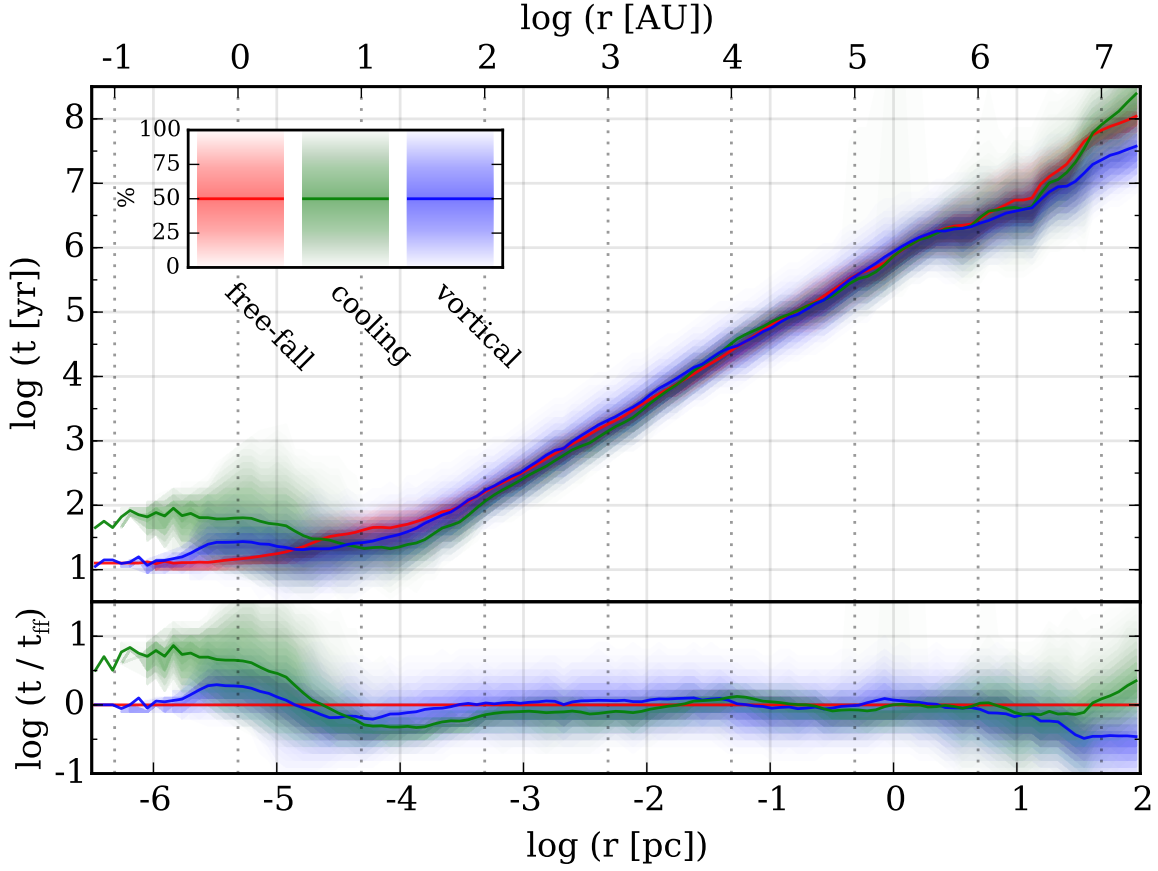


Figure 4. Top: radial profiles from the final output of the simulation with dust of the mass-weighted mean free-fall time (red), cooling time (green), and vortical time (blue). Bottom: ratio of cooling and vortical times to the free-fall time.

ulations. Clump identification (Smith et al. 2009; Turk et al. 2011b) proceeds by using a contouring algorithm to calculate the largest topologically disconnected structures that satisfy the following criterion:

$$KE + TE - \sum_i \Lambda_i t_{\text{dyn},i} < PE, \quad (4)$$

where KE, TE, and PE are the total kinetic, thermal, and potential energies of the clump, and Λ_i and $t_{\text{dyn},i}$ are the cooling rate and dynamical time for each member grid cell (Meece et al. 2014). As in Meece et al. (2014), we include the cooling term in Equation 4 to account for marginally unbound clumps that are rapidly cooling and, hence, expected to become gravitationally bound in the near future. In Figure 7, we show the number of clumps as a function of the minimum gas density within the clump. The minimum density within the clump effectively serves as the density at which the fragmentation event forming that clump occurred. In the simulation with dust, we identify 126 individual clumps, compared with 38 in the simulation without dust. Of the 38 clumps in the simulation without dust, 23 are at densities less than 10^{-17} g/cm^3 , similar to the simulation with dust, which has 21 in the same range. The masses of these are also similar, ranging from about $0.1 M_\odot$ up to about $1000 M_\odot$. The high density clumps ($\rho_{\text{min}} \gtrsim 10^{-13} \text{ g/cm}^3$) in the simulation with dust show a roughly log-normal distribution in masses, centered at $\sim 10^{-4} M_\odot$ and ranging from about $10^{-6} M_\odot$ to about $10^{-2} M_\odot$. The total gas mass within the central 50 AU is about $0.8 M_\odot$. While it is likely that a number of these may later

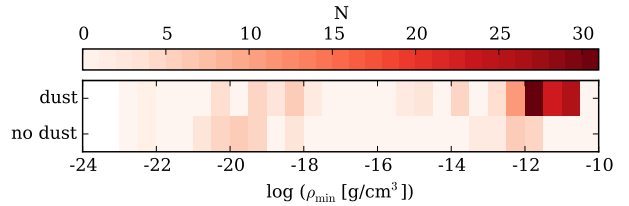


Figure 7. The number of bound clumps at a given threshold density (i.e., the minimum density of the clump) within the central 50 pc of each simulation.

merge, it is clear that the presence of dust significantly increases the degree of fragmentation during this phase of the collapse.

The increased fragmentation observed here can be conclusively attributed to the presence of dust by comparing the thermal state between the simulations with and without dust, as we do in Figure 8. The sharp decrease in temperature seen at high density, $n \gtrsim 10^{11} \text{ cm}^{-3}$, occurs when the dust and gas become thermally coupled and continuum emission from the dust is able to efficiently cool the gas. With dust present, gas in the density range, $10^7 \text{ cm}^{-3} \lesssim n \lesssim 10^{11} \text{ cm}^{-3}$, is also cooler by a factor of roughly 2 owing to the increased H_2 fraction from the availability of the dust-grain formation channel, as shown in Figure 9. These results are all in reasonable agreement with analogous one-zone models (Omukai 2000; Omukai et al. 2005; Schneider et al. 2006) and three-dimensional simulations (Clark et al. 2008; Dopcke et al.

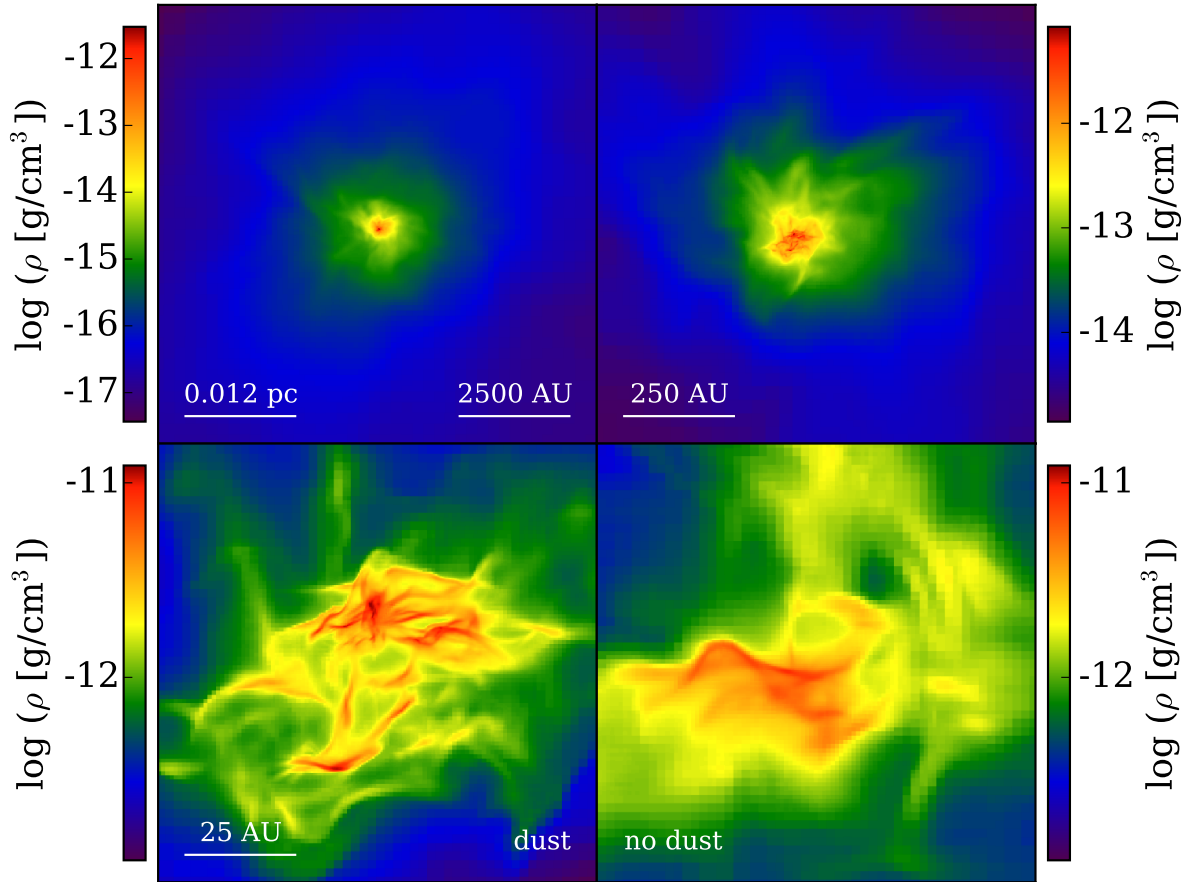


Figure 6. Mass-weighted density projections showing the collapse of the metal-enriched molecular cloud from the final output of the simulations. The bottom panels show the central, dense core of the simulation with (left) and without (right) dust. Distances shown are in the proper frame.

2011; Meece et al. 2014). The simulation without dust also shows a decrease in temperature at high density, albeit much less pronounced. As Figure 9 shows, this is due to the rapid increase in H_2 fraction caused by 3-body reactions becoming efficient. We note that this appears to happen somewhat later than in previous works (e.g., Omukai et al. 2005). However, it was shown by Meece et al. (2014) that the precise timing of collapse can significantly affect chemical evolution within the gas.

Finally, we briefly examine the velocity structure of the collapsing gas cloud in Figure 10. Here, as in Figures 4 and 5, we calculate the center of the cloud by creating a sphere of 100 pc centered on the halo, and iteratively recalculating the center of mass after decreasing the radius of the sphere by 10% until reaching a radius of 1 AU proper. For the velocity profiles, we subtract off the bulk velocity of the central 1 AU. We define the rotational velocity as the component that is orthogonal to both the radial and angular momentum vectors, where the angular momentum vector is calculated from the central 1 AU. The cloud is dominated by turbulent, or at least unordered, motion as the variance of the velocity magnitude (minus the bulk velocity of the center) is higher than both the radial and rotational components at all radii. At large radii, the velocity variance is between 1.5 and 2 times the sound speed and closely follows the sound speed at lower radii, only exceeding it at $r \sim 10$ AU where the cooling leads to rapid cooling. Though less than the variance at all radii, there is still a significant infall component that is generally trans-sonic. We find that in the simulation

without dust where the gas temperature slightly higher, the infall is similarly raised. The gas shows almost no coherent rotation with an average rotational velocity that is near zero at virtually all radii. This is not simply an effect of where we have chosen to calculate the angular momentum vector as we find that calculating it at $r = 10$ and 100 AU gives qualitatively similar results.

3.4 The Bigger Picture for Metal-Enriched Star Formation

The gravitational binding energy of mini-halos is well below the energy of even a standard core-collapse supernova. As such, it will be some time before metal-enriched stars are able to form in-situ from self-enrichment of the progenitor halos that form Pop III stars. However, just two Pop III stars have enriched a considerable amount of space and material by $z \sim 16.6$, when this simulation stops. In Figures 11 and 12, we show the volume and mass enriched to metallicities high enough to transition to a metal-enriched star formation mode. Roughly 1% of the mass and just under 1% of the volume within the high-resolution region of the simulation are enriched to a metallicity of $10^{-5} Z_{\odot}$ by the final output. Only a small fraction of the metals created in the two supernovae will be captured by nearby halos and be incorporated into stars by the time the target halo has assembled at $z = 10$ with a total mass of $\sim 2 \times 10^7 M_{\odot}$, about 250 Myr from the current time in the simulation. If metal-enriched star formation occurs on free-fall timescales, this 250 Myr time period corresponds to a density of roughly 10^{-25}

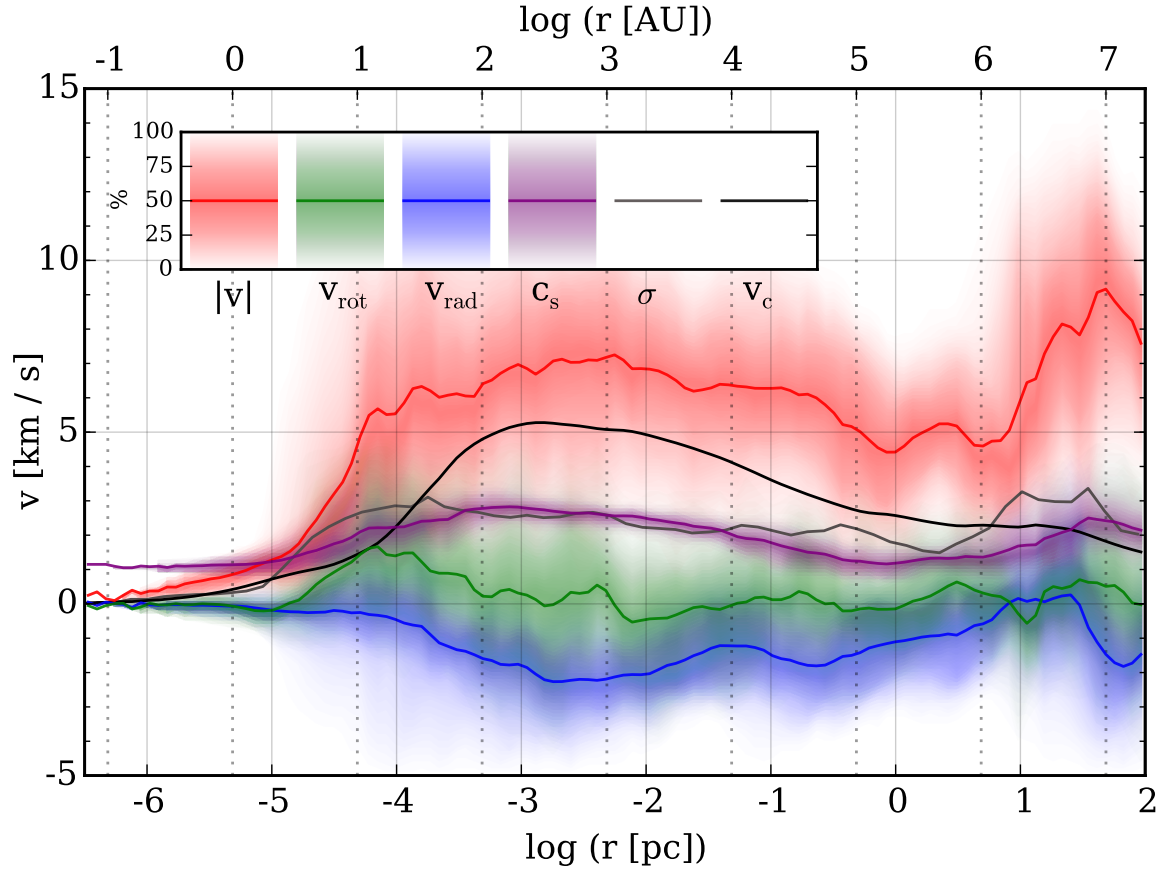


Figure 10. Radial profiles of the mass-weighted, mean velocity magnitude (red), rotational velocity (green), radial velocity (blue), and sound speed (purple). The variance of the total velocity is shown in grey and the circular velocity corresponding to the enclosed mass is shown in black.

g/cm^3 . Following this assumption, we can estimate the number of additional halos externally enriched by these two Pop III supernovae that will be able to form Pop II stars in this time period by searching for all the halos with metallicities of at least $10^{-6} Z_{\odot}$ in gas with $\rho \geq 10^{-25} \text{ g/cm}^3$.

In Figure 13, we show the results of this attempt to predict the future. In this exercise, we consider halos with masses as low as $10^3 M_{\odot}$. We identify 21 halos in which Pop II stars could form before the target halo has assembled. In cases where the metallicity is less than $\sim 10^{-4} Z_{\odot}$, gas-phase metal cooling will be insufficient at low densities, requiring a critical H_2 fraction in a scenario analogous to the filtering mass for Pop III star formation (Tegmark et al. 1997; Yoshida et al. 2003). To account for this, we require halos with $Z < 10^{-4} Z_{\odot}$ to have a minimum mass of $10^5 M_{\odot}$. In other words, halos with $M < 10^5 M_{\odot}$ must have metallicities of at least $10^{-4} Z_{\odot}$ such that they are able to cool via metal lines. This constraint lowers the number of candidate halos to 16. Of these 16 halos, 7 have masses of $10^3 M_{\odot} < M < 10^4 M_{\odot}$, 6 have masses of $10^4 M_{\odot} < M < 10^5 M_{\odot}$, and 3 have masses of $10^5 M_{\odot} < M < 10^6 M_{\odot}$. Despite having a 66 Myr head start, only 1 of the 16 candidate halos exists in the region enriched by the first of the two supernovae. In fact, this halo is the original host of the Pop III star. Out of random chance, the halo hosting the first Pop III star has significantly fewer neighbors than that of the second Pop III star. It has been approximately 96 Myr since the explosion of the first supernova. That this halo has not yet recovered is consistent

with Jeon et al. (2014), who find a recovery time of 140 Myr for a $3 \times 10^5 M_{\odot}$ halo experiencing a 10^{51} erg explosion. The lower panels of Figure 13 show that the halo hosting the second Pop III star (as well as the action halo) formed in a significantly denser region with many more neighboring halos. Out of the $22.39 M_{\odot}$ of metals created, about $1.8 M_{\odot}$ have been captured by neighboring halos. It is important to note that as metal-enriched stars form within region b of Figure 13, their feedback may influence other nearby candidate halos, either inhibiting star formation with radiation or contributing additional metals via supernovae. Thus, the resulting star formation in this region may be slightly different from the picture presented here, although it is difficult to know for sure without running the simulation into the future including Pop II star particles.

What is most striking is the range in metallicities resulting from a single enrichment event. A total of 7 halos have metallicities in their dense gas ($\rho \geq 10^{-25} \text{ g/cm}^3$) of at least $10^{-3} Z_{\odot}$, with a single halo as high as $0.1 Z_{\odot}$. The halo with the highest metallicity is, in fact, the combined action/Pop III halo, represented in Figure 13 as the large, red circle in the center of region b. The core of the Pop III halo is just barely visible to the lower-right of the main core of this structure. Just after the collision with the blast-wave but before encountering the Pop III halo, the action halo experiences a major merger. The final object, including the not yet totally merged Pop III halo, has a mass of $9.8 \times 10^5 M_{\odot}$. Interestingly, it seems that it will likely form both the lowest and highest metallicity Pop II stars from the metals created thus far. More im-

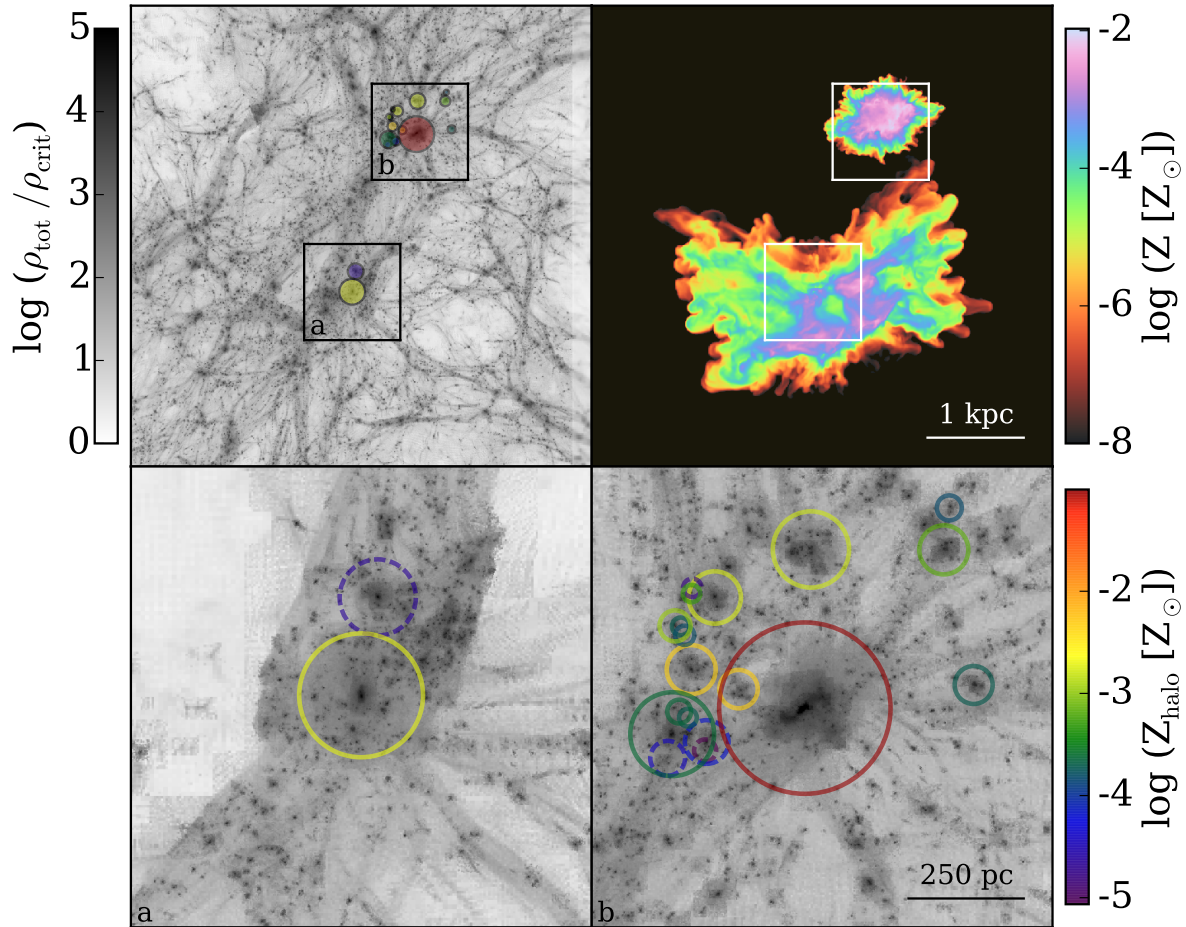


Figure 13. Top panels show projections of overdensity (left) and metallicity (right) in a region minimally containing all of the metals produced in the simulation. Bottom panels show projections of the regions surrounding each of the two supernova events. Region a contains the first Pop III star to form and region b contains the second as well as the action halo. The locations of halos with metallicities of at least $10^{-6} Z_{\odot}$ in dense gas ($\rho \geq 10^{-25} \text{ g/cm}^3$). The size and color of the circles indicate the virial radii and peak dense gas metallicities, respectively. The dashed lines indicate halos with masses less than $10^5 M_{\odot}$ and metallicities below $10^{-4} Z_{\odot}$ which may be unable to cool.

portantly, the picture presented here shows that *the first generation of metal-enriched stars was highly heterogeneous in metallicity, encompassing significantly more than just the most metal-poor stars.*

4 DISCUSSION

4.1 Implications

The one-zone collapse models with their extremely sophisticated chemistry networks (Omukai 2000; Omukai et al. 2005, and related works) have paved the way toward understanding the required conditions for fragmentation from the perspective of the ability of low metallicity gas to cool. The simplicity of the collapse model has enabled the exploration of a large parameter space of non-solar abundance patterns motivated by Pop III supernova yield predictions (Schneider et al. 2006) and varying levels of dust (Schneider et al. 2012). Encouragingly, the idealized three-dimensional simulations (Bromm et al. 2001; Smith & Sigurdsson 2007; Clark et al. 2008; Smith et al. 2009; Dopcke et al. 2011, 2013; Meece et al. 2014) have confirmed that the thermal evolution predicted by these models can, indeed, induce fragmentation provided there is a small

degree of turbulence to seed density perturbations. This is particularly interesting given that the recently discovered most metal-poor star, SMSS J031300.36-670839.3 (Keller et al. 2014), has abundance patterns compatible with the yield of a single Pop III supernova (Keller et al. 2014; Marassi et al. 2014). Additionally, Marassi et al. (2014) have shown that, under a range of dust abundances, a collapsing gas-cloud with the chemical composition of SMSS J031300.36-670839.3 would have undergone low-mass fragmentation. What has been missing from this picture is a means to implant such low metallicities into a star forming environment. We have provided such a mechanism in this work.

The frequency with which this mechanism operates is uncertain, although it is also encouraging that Greif et al. (2010) appear to have identified a similar situation, albeit with a higher metallicity ($Z \sim 2 \times 10^{-4} Z_{\odot}$). We have, so far, only followed this one occurrence, although we identify a number of other externally enriched halos that could potentially form stars with metals from a single supernova. However, it is clear that the number of halos externally enriched by a given Pop III supernova will vary greatly. For example, the region around the first Pop III star in our simulation has no viable externally enriched halo candidates and will see second generation star formation only after the Pop III halo itself recovers.

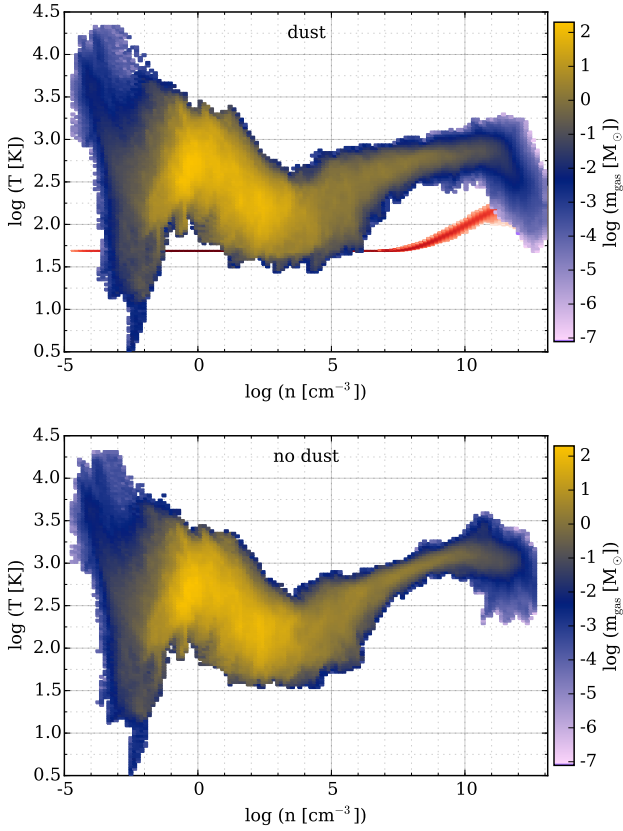


Figure 8. Phase plots of the gas mass in bins of number density and temperature for the simulation with (top) and without (bottom) dust. In the top panel, the red shows the analogous distribution for the dust temperature.

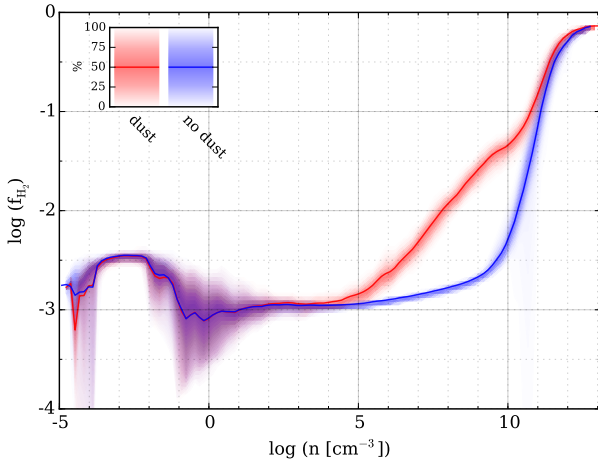


Figure 9. Profiles of the mass-weighted average H_2 fraction as a function of number density for the two simulations.

By contrast, the region around the second Pop III star has a number of such candidates. To first order, the likelihood of the external enrichment mechanism depends on the average separation of Pop III star-forming halos from mini-halos that have yet to undergo star formation. We provide a crude estimate of this in Figure 14. Using the exploratory simulation, we identify all halos with masses greater than $10^5 M_\odot$ and calculate the distance to the nearest halo with a mass in the range of $10^5 M_\odot \leq M \leq 5 \times 10^5 M_\odot$. The

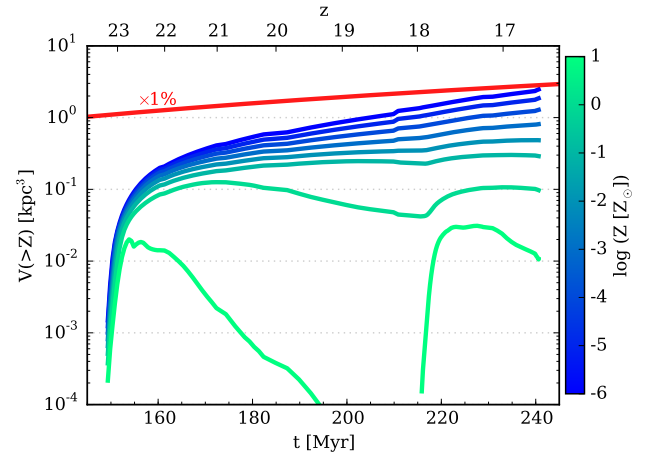


Figure 11. The volume within the simulation enriched to at least a given metallicity as a function of redshift. The different colors show metallicities ranging from $Z = 10^{-6} Z_\odot$ (blue) to $10 Z_\odot$ (green) increasing by factors of ten. The red line shows 1% of the total volume of the high resolution region.

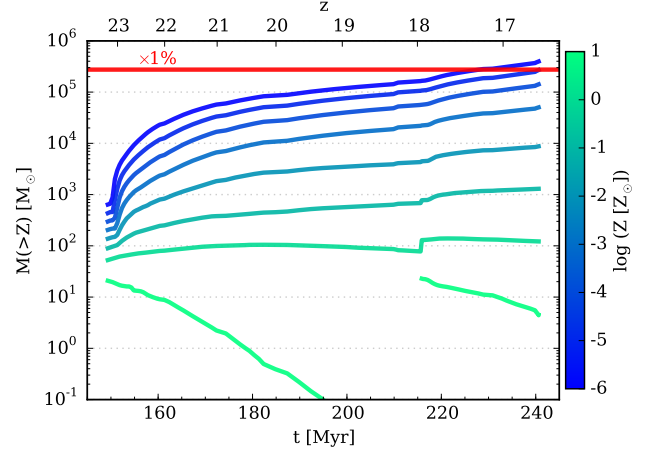


Figure 12. The mass of gas enriched to at least a given metallicity as a function of redshift. The different colors show metallicities ranging from $Z = 10^{-6} Z_\odot$ (blue) to $10 Z_\odot$ (green) increasing by factors of ten. The red line shows 1% of the total baryon mass within the high resolution region. Note, the refinement region is in a large-scale overdensity and has roughly 2.8 times more mass than an average region of that size.

former group is assumed to have a high probability of forming a Pop III star, where the latter may be just about to do so. We allow the mass ranges to overlap noting that the action halo is actually more massive than the Pop III halo. During the period from $z = 20$ to $z = 10$, the average separation of these pairs is roughly 500 pc and evolves very little. The high resolution region of the simulation shows a similar evolution but with a slightly lower value of about 300–400 pc owing to the fact that it is located within a large-scale overdensity. The distance between the Pop III halo and the action halo is slightly more than 1 standard deviation lower than the average pair separation within the full simulation volume. This suggests that the external enrichment mechanism is a non-negligible component of low-metallicity star formation. Jeon et al. (2014) find that the recovery time for mini-halos with $M \lesssim 5 \times 10^5 M_\odot$ (similar to the Pop III star-forming halos in our simulations) is of the order of 100 Myr. In the simulations presented here, the time between

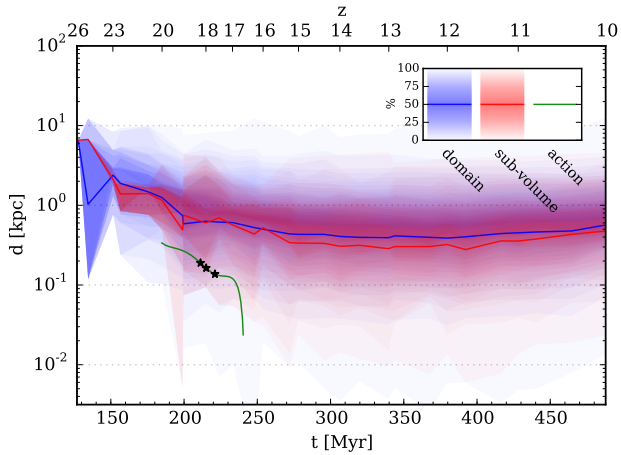


Figure 14. The blue line and shaded region shows the average distance between halos with mass, $M \geq 10^5 M_{\odot}$, and the nearest halo with mass, $10^5 M_{\odot} \leq M \leq 5 \times 10^5 M_{\odot}$ as a function of redshift for the entire simulation volume. The red line and shaded region shows the measurement for just the high resolution region. The green line shows the distance between the action halo and the Pop III star-forming halo. The three black stars indicate the moments when the Pop III star forms, explodes, and when the supernova blast-wave collides with the action halo.

the explosion of the second supernova and the collapse of metal-enriched gas is roughly 25 Myr. The shorter timescale is not surprising, as the mixing of metals into a nearby halo will occur early on when the blast-wave is still moving outward quickly. Thus, if the conditions are right for the external enrichment mechanism to occur, it should typically produce metal-enriched stars before they can form from fallback of metals onto the Pop III halo.

Finally, the candidate halos surrounding the second Pop III star have a wide range of metallicities, from just over $10^{-4} Z_{\odot}$ to nearly $10^{-2} Z_{\odot}$. This range of metallicities is, itself, a striking result as it implies that there may be stars that are only moderately metal-poor by observational standards (with, e.g., thousands existing in the SDSS SEGUE sample) yet trace a single progenitor. This could present a new opportunity to gain access to the Pop III IMF, although one that will certainly not be without its own challenges.

4.2 Caveats and Limitations

We make strong assumptions about the properties of the metals and dust grains in these simulations. We assume that gas-phase metals have a solar abundance pattern and that the dust grains are of a composition, size distribution, and fraction of total metal mass identical to the interstellar medium of the Milky Way. While these assumptions are not explicitly correct, the thermal evolution we observe is still in reasonable agreement with studies that use realistic abundance patterns and dust properties (e.g. Schneider et al. 2006, 2012; Marassi et al. 2014). We also assume that the dust grain population is static after the initial grain formation, although it has been shown recently that grains can continue to grow during collapse and that their effects can be important even when the initial depletion fraction is very small (Nozawa et al. 2012; Chiaki et al. 2013, 2014). These effects, along with more realistic abundance patterns, will be important to consider in the future when these simulations can be carried to the point where an IMF can be reasonably extrapolated from their final state. However, given the current lack of understanding of the physical origin of the stellar IMF, such an

exercise is not warranted at this time. In relation to the chemistry model employed here, the primary goal of this work is to show that the high density cooling phase associated with dust can induce fragmentation in realistic conditions.

We have chosen the formation of a $40 M_{\odot}$ Pop III star followed by a 10^{51} erg core-collapse supernova as the sole outcome of the collapse of metal-free gas. Since this work deals with enrichment of star forming gas by a single supernova, this assumption is as valid as choosing from a realistic IMF (e.g. Hirano et al. 2015) provided that the mass chosen is plausible within that IMF, which in this case is true. However, given the range of alternative Pop III explosion scenarios, such as energetic hypernova (Nomoto et al. 2006) and pair-instability supernova (Heger & Woosley 2002), determining the robustness of the external enrichment mechanism to different explosion energies and yields has significant merit and is a topic we will explore in a future study. For example, Cooke & Madau (2014) claim that the lack of observational evidence for Pop III pair-instability supernova does not necessarily rule out their existence entirely. Instead, they argue that the transition to Pop II star formation may simply be dominated by low energy supernovae whose ejecta fall back quickly while pair-instability events are masked by the fact that they evacuate their host halos and have very long recovery times. However, if pair-instability supernovae can just as easily give rise to the external enrichment mechanism presented here, it could present a problem for this explanation.

Given the nature of our code, which is both grid-based and uses adaptive mesh refinement, it is possible that the mixing of metals is artificially enhanced in our second-generation halo. This is a known property of grid-based codes (e.g., Wadsley et al. 2008; Joggerst et al. 2014), and must be kept in mind when interpreting results such as those presented in Figure 3. In this particular simulation, however, there is reason to believe that numerical mixing is not the origin of the uniform metallicity seen in the center of our second-generation halo. This is due to the nature of the fluid flow in the halo, which is highly turbulent. Turbulence results in the efficient mixing of metals over the length scales of the turbulent cascade on the scale of a few local eddy turnover times, which are comparable to the local dynamical time in supersonic turbulence (Balsara & Kim 2005; Pan & Scannapieco 2010). As can be seen in Figure 4, the dynamical, cooling, and vortical (i.e., turbulence) scales are quite comparable over the inner parsec of the second-generation halo, suggesting that the gas is well-mixed. This thorough mixing may also be observed in nature – Karlsson et al. (2012) shows the tentative existence of a dissolved star cluster with $[\text{Fe}/\text{H}] \simeq -2.7$ in the Sextans dSph galaxy. This star cluster was found using chemical tagging, and found a handful of very old stars that are highly clustered in a multi-dimensional chemical abundance space. This clumping indicates chemical homogeneity in the gas cloud out of which these stars formed, which is estimated to be substantially more massive than the one under consideration in our calculation, and supports the assertion that gas should be well-mixed due to turbulent processes.

5 SUMMARY AND CONCLUSIONS

We present the first results from a study designed to characterize the physical conditions associated with the transition from Pop III to Pop II star formation. We have simulated the formation of the first Pop II stars in the Universe in a single, coherent simulation beginning from cosmological initial conditions. The simulations have a dark matter particle mass of just under $1.3 M_{\odot}$, allowing us to

well-resolve the small ($\text{few} \times 10^5 M_{\odot}$) mini-halos that host the first stars. We insert $40 M_{\odot}$ Pop III star particles in metal-free molecular clouds that have evolved past the loitering phase and simulate their main-sequence lives with radiation hydrodynamics. Each Pop III star explodes in a 10^{51} erg core-collapse supernova and we follow the non-uniform enrichment of the IGM and turbulent mixing that occurs as the blast-wave washes over neighboring halos. The simulation ends when metal-enriched gas is able to cool and collapse into dense, pre-stellar cores. The key results from this work are as follows:

(i) The first metal-enriched stars form at $z \sim 16.6$ when a single Pop III supernova blast-wave washes over a neighboring mini-halo of comparable size that has yet to form its own Pop III star. Turbulence caused by the virialization of the halo and collision with the blast-wave allows metals to reach the interior of the halo. The gas within 0.01 pc of the dense core is uniformly mixed to a metallicity of $\sim 2 \times 10^{-5} Z_{\odot}$.

(ii) Because the metallicity of the dense core is less than the gas-phase critical metallicity ($Z_{cr} \sim 10^{-3.5} Z_{\odot}$), the thermal evolution of the gas as it collapses is similar to the metal-free case until dust cooling becomes efficient at $n \sim 10^{12} \text{ cm}^{-3}$. At this point, a sharp drop in temperature occurs that induces significant fragmentation into many small clumps with masses of roughly $10^{-4} M_{\odot}$. We run a second version of this simulation without dust and observe greatly reduced fragmentation.

(iii) The velocity structure of the gas is dominated by turbulent motions at all scales, from ~ 100 pc (the outskirts of the halo) down to a few AU. The turbulent velocity, defined as the variance in the total velocity magnitude, roughly follows the local sound. At large radii, where efficient mixing occurs, the turbulent velocity reaches as high as Mach 2. The radial velocity also follows the local sound speed, but is somewhat smaller. The gas shows virtually no coherent rotation on any scale.

(iv) By the end of the simulation, two Pop III supernovae have exploded in separate regions. The region in which the first supernova explodes has relatively few halos. As a result, only the original host halo of the Pop III star exists as a potential site for second generation star formation in this region. However, 15 halos exist in the region around the second supernova that have metal-enriched gas dense enough to form stars by the time that the larger structure encompassing them has assembled at $z = 10$. Not counting the Pop III host halo, these halos have metallicities ranging from slightly over $10^{-4} Z_{\odot}$ to nearly $10^{-2} Z_{\odot}$. Thus, the first Pop II stars may have had a wide range of metallicities.

We have identified one pathway, however small, from the exoticism of the early Universe to the normalcy of the present day. It is likely that multiple scenarios contributed to the transition from Pop III to Pop II star formation. While its overall contribution to Pop II star formation is probably minor, the external enrichment mechanism offers the best explanation for the origin of the most metal-poor stars observed and the clearest window into IMF of the first stars.

ACKNOWLEDGMENTS

We are grateful to the anonymous referee whose comments helped strengthen the manuscript. This research is part of the Blue Waters sustained-petascale computing project, which is supported by the NSF (award number ACI-1238993) and the state of Illinois.

Blue Waters is a joint effort of the University of Illinois at Urbana-Champaign and the National Center for Supercomputing Applications. The simulations described by this paper were run using an NSF PRAC allocation (award number OCI-0832662). B.W.O. was supported in part by the MSU Institute for Cyber-Enabled Research and the NSF through grant PHY-0941373 and by NASA through grant NNX12AC98G and Hubble Theory Grant HST-AR-13261.01-A. B.W.O was supported in part by the sabbatical visitor program at the Michigan Institute for Research in Astrophysics (MIRA) at the University of Michigan in Ann Arbor, and gratefully acknowledges their hospitality. This research was supported by National Science Foundation (NSF) grant AST-1109243 to M.L.N. J.H.W. acknowledges support from NSF grants AST-1211626 and AST-1333360 and Hubble Theory Grant HST-AR-13895.001-A. The analysis presented here made extensive use of new features developed for version 3.0 of yt. B.D.S. wishes to thank all the members of the yt community for their hard work, which helped to enable this research. This research has made use of NASA’s Astrophysics Data System Bibliographic Services. Computations and associated analysis described in this work were performed using the publicly available Enzo code and the yt analysis toolkit, which are the products of collaborative efforts of many independent scientists from numerous institutions around the world. Their commitment to open science has helped make this work possible.

REFERENCES

- Abel T., Anninos P., Zhang Y., Norman M. L., 1997, *New A*, 2, 181
 Abel T., Bryan G. L., Norman M. L., 2002, *Science*, 295, 93
 Anninos P., Zhang Y., Abel T., Norman M. L., 1997, *New A*, 2, 209
 Balsara D. S., Kim J., 2005, *ApJ*, 634, 390
 Barkana R., Loeb A., 2001, *Phys. Rep.*, 349, 125
 Bastian N., Covey K. R., Meyer M. R., 2010, *ARA&A*, 48, 339
 Behroozi P. S., Wechsler R. H., Wu H. Y., 2013a, *ApJ*, 762, 109
 Behroozi P. S., Wechsler R. H., Wu H. Y., Busha M. T., Klypin A. A., Primack J. R., 2013b, *ApJ*, 763, 18
 Berger M. J., Colella P., 1989, *Journal of Computational Physics*, 82, 64
 Bromm V., Larson R. B., 2004, *ARA&A*, 42, 79
 Bromm V., Loeb A., 2003, *Nature*, 425, 812
 Bromm V., Ferrara A., Coppi P. S., Larson R. B., 2001, *MNRAS*, 328, 969
 Bromm V., Coppi P. S., Larson R. B., 2002, *ApJ*, 564, 23
 Bromm V., Yoshida N., Hernquist L., McKee C. F., 2009, *Nature*, 459, 49
 Bryan G. L., Norman M. L., O’Shea B. W., Abel T., Wise J. H., Turk M. J., Enzo Collaboration, 2014, *ApJ.S.S.*, 211, 19
 Cen R., Riquelme M. A., 2008, *ApJ*, 674, 644
 Chen P., Wise J. H., Norman M. L., Xu H., O’Shea B. W., 2014, *ApJ*, 795, 144
 Chiaki G., Nozawa T., Yoshida N., 2013, *ApJ*, 765, L3
 Chiaki G., Schneider R., Nozawa T., Omukai K., Limongi M., Yoshida N., Chieffi A., 2014, *MNRAS*, 439, 3121
 Ciardi B., Ferrara A., 2005, *Space Sci. Rev.*, 116, 625
 Clark P. C., Glover S. C. O., Klessen R. S., 2008, *ApJ*, 672, 757
 Clark P. C., Glover S. C. O., Smith R. J., Greif T. H., Klessen R. S., Bromm V., 2011, *Science*, 331, 1040
 Cooke R. J., Madau P., 2014, *ApJ*, 791, 116
 Dopcke G., Glover S. C. O., Clark P. C., Klessen R. S., 2011, *ApJ*, 729, L3
 Dopcke G., Glover S. C. O., Clark P. C., Klessen R. S., 2013, *ApJ*, 766, 103
 Efsthathiou G., Davis M., White S. D. M., Frenk C. S., 1985, *ApJS*, 57, 241
 Eisenstein D. J., Hu W., 1999, *ApJ*, 511, 5
 Federrath C., Sur S., Schleicher D. R. G., Banerjee R., Klessen R. S., 2011, *ApJ*, 731, 62
 Ferland G. J. et al., 2013, *Rev. Mexicana Astron. Astrofis.*, 49, 137

- Glover S., 2005, *Space Sci. Rev.*, 117, 445
- Greif T. H., Johnson J. L., Bromm V., Klessen R. S., 2007, *ApJ*, 670, 1
- Greif T. H., Johnson J. L., Klessen R. S., Bromm V., 2008, *MNRAS*, 387, 1021
- Greif T. H., Glover S. C. O., Bromm V., Klessen R. S., 2010, *ApJ*, 716, 510
- Greif T. H., Springel V., White S. D. M., Glover S. C. O., Clark P. C., Smith R. J., Klessen R. S., Bromm V., 2011, *ApJ*, 737, 75
- Hahn O., Abel T., 2011, *MNRAS*, 415, 2101
- Hartwig T., Bromm V., Klessen R. S., Glover S. C. O., 2015, *MNRAS*, 447, 3892
- Heger A., Woosley S. E., 2002, *ApJ*, 567, 532
- Hirano S., Hosokawa T., Yoshida N., Umeda H., Omukai K., Chiaki G., Yorke H. W., 2014, *ApJ*, 781, 60
- Hirano S., Hosokawa T., Yoshida N., Omukai K., Yorke H. W., 2015, *MNRAS*, 448, 568
- Hockney R. W., Eastwood J. W., 1988, *Computer simulation using particles*
- Hosokawa T., Omukai K., Yoshida N., Yorke H. W., 2011, *Science*, 334, 1250
- Jappsen A. K., Glover S. C. O., Klessen R. S., Mac Low M. M., 2007, *ApJ*, 660, 1332
- Jappsen A. K., Klessen R. S., Glover S. C. O., Mac Low M. M., 2009a, *ApJ*, 696, 1065
- Jappsen A. K., Mac Low M. M., Glover S. C. O., Klessen R. S., Kitsionas S., 2009b, *ApJ*, 694, 1161
- Jeon M., Pawlik A. H., Bromm V., Milosavljević M., 2014, *MNRAS*, 444, 3288
- Joggerst C. C. et al., 2014, *Journal of Computational Physics*, 275, 154
- Johnson J. L., 2014, *ArXiv e-prints* (1411.4189)
- Karlsson T., Bland-Hawthorn J., Freeman K. C., Silk J., 2012, *ApJ*, 759, 111
- Keller S. C. et al., 2014, *Nature*, 506, 463
- Kitayama T., Yoshida N., 2005, *ApJ*, 630, 675
- Komatsu E., Smith K. M., Dunkley J., Bennett C. L., Gold B., Hinshaw, 2011, *ApJS*, 192, 18
- Kroupa P., 2002, *Science*, 295, 82
- Maio U., Khochfar S., Johnson J. L., Ciardi B., 2011, *MNRAS*, 414, 1145
- Marassi S., Chiaki G., Schneider R., Limongi M., Omukai K., Nozawa T., Chieffi A., Yoshida N., 2014, *ApJ*, 794, 100
- Meece G. R., Smith B. D., O'Shea B. W., 2014, *ApJ*, 783, 75
- Nomoto K., Tominaga N., Umeda H., Kobayashi C., Maeda K., 2006, *Nuclear Physics A*, 777, 424
- Norris J. E. et al., 2013, *ApJ*, 762, 28
- Nozawa T., Kozasa T., Nomoto K., 2012, *ApJ*, 756, L35
- Omukai K., 2000, *ApJ*, 534, 809
- Omukai K., Tsuribe T., Schneider R., Ferrara A., 2005, *ApJ*, 626, 627
- O'Shea B. W., Norman M. L., 2007, *ApJ*, 654, 66
- O'Shea B. W., Norman M. L., 2008, *ApJ*, 673, 14
- O'Shea B. W., Abel T., Whalen D., Norman M. L., 2005, *ApJ*, 628, L5
- Pan L., Scannapieco E., 2010, *ApJ*, 721, 1765
- Pollack J. B., Hollenbach D., Beckwith S., Simonelli D. P., Roush T., Fong W., 1994, *ApJ*, 421, 615
- Richardson M. L. A., Scannapieco E., Gray W. J., 2013, *ApJ*, 778, 80
- Ripamonti E., Abel T., 2006, *The Formation of Primordial Luminous Objects*. pp. 239–289
- Ritter J. S., Safrank-Shrader C., Gnat O., Milosavljević M., Bromm V., 2012, *ApJ*, 761, 56
- Ritter J. S., Sluder A., Safrank-Shrader C., Milosavljevic M., Bromm V., 2014, *ArXiv e-prints* (1408.0319)
- Safrank-Shrader C., Milosavljević M., Bromm V., 2014a, *MNRAS*, 440, L76
- Safrank-Shrader C., Milosavljević M., Bromm V., 2014b, *MNRAS*, 438, 1669
- Safrank-Shrader C., Montgomery M., Milosavljevic M., Bromm V., 2015, *ArXiv e-prints* (1501.03212)
- Schaerer D., 2002, *A&A*, 382, 28
- Schneider R., Omukai K., Inoue A. K., Ferrara A., 2006, *MNRAS*, 369, 1437
- Schneider R., Omukai K., Bianchi S., Valiante R., 2012, *MNRAS*, 419, 1566
- Smith B., Sigurdsson S., Abel T., 2008, *MNRAS*, 385, 1443
- Smith B. D., Sigurdsson S., 2007, *ApJ*, 661, L5
- Smith B. D., Turk M. J., Sigurdsson S., O'Shea B. W., Norman M. L., 2009, *ApJ*, 691, 441
- Stacy A., Bromm V., 2014, *ApJ*, 785, 73
- Stacy A., Greif T. H., Bromm V., 2010, *MNRAS*, 403, 45
- Susa H., Hasegawa K., Tominaga N., 2014, *ApJ*, 792, 32
- Tegmark M., Silk J., Rees M. J., Blanchard A., Abel T., Palla F., 1997, *ApJ*, 474, 1
- Truelove J. K., Klein R. I., McKee C. F., Holliman II J. H., Howell L. H., Greenough J. A., 1997, *ApJ*, 489, L179+
- Turk M. J., Abel T., O'Shea B., 2009, *Science*, 325, 601
- Turk M. J., Norman M. L., Abel T., 2010, *ApJ*, 725, L140
- Turk M. J., Clark P., Glover S. C. O., Greif T. H., Abel T., Klessen R., Bromm V., 2011a, *ApJ*, 726, 55
- Turk M. J., Smith B. D., Oishi J. S., Skory S., Skillman S. W., Abel T., Norman M. L., 2011b, *ApJS*, 192, 9
- Turk M. J., Oishi J. S., Abel T., Bryan G. L., 2012, *ApJ*, 745, 154
- Wadsley J. W., Veeravalli G., Couchman H. M. P., 2008, *MNRAS*, 387, 427
- Whalen D., Abel T., Norman M. L., 2004, *ApJ*, 610, 14
- Whalen D., van Veelen B., O'Shea B. W., Norman M. L., 2008, *ApJ*, 682, 49
- Wise J. H., Abel T., 2007, *ApJ*, 665, 899
- Wise J. H., Abel T., 2008, *ApJ*, 685, 40
- Wise J. H., Abel T., 2011, *MNRAS*, 414, 3458
- Wise J. H., Abel T., Turk M. J., Norman M. L., Smith B. D., 2012a, *MNRAS*, 427, 311
- Wise J. H., Turk M. J., Norman M. L., Abel T., 2012b, *ApJ*, 745, 50
- Wise J. H., Demchenko V. G., Halicek M. T., Norman M. L., Turk M. J., Abel T., Smith B. D., 2014, *MNRAS*, 442, 2560
- Wolcott-Green J., Haiman Z., Bryan G. L., 2011, *MNRAS*, 418, 838
- Woodward P., Colella P., 1984, *Journal of Computational Physics*, 54, 115
- Xu H., Wise J. H., Norman M. L., 2013, *ApJ*, 773, 83
- Yoshida N., Abel T., Hernquist L., Sugiyama N., 2003, *ApJ*, 592, 645
- Yoshida N., Omukai K., Hernquist L., Abel T., 2006, *ApJ*, 652, 6